

Multiresolution Detection of Spiculated Lesions in Digital Mammograms

Sheng Liu, *Member, IEEE*, Charles F. Babbs, and Edward J. Delp, *Fellow, IEEE*

Abstract—In this paper, we present a novel multiresolution scheme for the detection of spiculated lesions in digital mammograms. First, a multiresolution representation of the original mammogram is obtained using a linear phase nonseparable two-dimensional (2-D) wavelet transform. A set of features is then extracted at each resolution in the wavelet pyramid for every pixel. This approach addresses the difficulty of predetermining the neighborhood size for feature extraction to characterize objects that may appear in different sizes. Detection is performed from the coarsest resolution to the finest resolution using a binary tree classifier. This top-down approach requires less computation by starting with the least amount of data and propagating detection results to finer resolutions. Experimental results using the MIAS image database have shown that this algorithm is capable of detecting spiculated lesions of very different sizes at low false positive rates.

Index Terms—Binary classification tree, digital mammogram, feature analysis, multiresolution, spiculated lesion.

I. INTRODUCTION

BREAST cancer is the most common form of cancer in American women and the second major cause of death after lung cancer [1]. It is a serious health problem in the U.S., the incidence of which continues to rise [2]. Mammography is currently the best technique for reliable detection of early, non-palpable, potentially curable breast cancer [3]. The mortality rate from this disease decreased for the first time in 1995, due in part to the increasing utilization of screening mammography [2]. However, radiologists vary in their interpretation of mammograms. In addition, the interpretation is a repetitive task that requires much attention to minute detail. Therefore, in the past several years there has been great interest in the use of image processing and analysis techniques [4]–[9] for automated tumor detection in digital mammograms. The goal has been to increase diagnostic accuracy as well as the reproducibility of mammographic interpretation.

Among breast abnormalities, spiculated masses having a stellate appearance in mammograms are highly suspicious indica-

tors of breast cancer [1]. Their central masses are usually irregular with ill-defined borders. Their sizes vary from a few millimeters to several centimeters in diameter. Computer aided diagnosis of digital mammograms generally consists of feature extraction followed by classification [4]. For spiculated lesions, Kegelmeyer, *et al.* [8], [10] extracted a five-dimensional (5-D) feature vector for each pixel which included the standard deviation of the edge orientation histogram (ALOE) and the output of four spatial filters. Each feature vector was then classified using a binary decision tree. They chose the window size for obtaining the ALOE feature to be 4 cm so that it was large enough to encompass all of the spiculated lesions in their data. Karssemeijer and Brake [11] investigated a method based on statistical analysis of a map of edge orientations. Two features were derived from the edge orientation map that were used to classify suspicious regions. To cover the range of sizes of the spicules in their data set, edge orientations were derived at three spatial scales and the one with the maximum absolute value was used. In general, it has proved difficult to determine the size of the neighborhood that should be used to extract local features of spiculated lesions. If the neighborhood is too large, small lesions may be missed, while if the neighborhood is too small, parts of large lesions may be missed.

In this paper, we present a multiresolution scheme for the detection of spiculated lesions in mammograms that specifically addresses this difficulty of predetermining the neighborhood size for feature extraction. The system diagram is shown in Fig. 1. We first obtain a multiresolution representation of the original mammogram using a linear phase nonseparable two-dimensional (2-D) wavelet transform. Features that are designed to differentiate spiculated lesions from normal structures are then extracted for every pixel at each resolution. Detection is performed from the coarsest resolution to the finest resolution using a binary tree classifier. There is a fundamental difference in our method than other approaches, which is also the novelty of our algorithm, in that we extract and classify features at multiple resolutions, hence overcoming the difficulty of choosing a neighborhood size *a priori* to capture tumors of varying sizes. Furthermore, the top-down classification we use requires less computation by starting with the coarsest resolution image (least amount of data) and propagating detection results to finer resolutions.

In Section II, we describe the multiresolution decomposition method. In Section III, we discuss the mammographic features used to characterize spiculated lesions of different sizes at various resolutions. The top-down classification approach is discussed in Section IV. Finally, we present experimental results and discussion in Section V.

Manuscript received June 8, 1998; revised October 17, 2000. This work was supported by Grant CA62243 from the National Institutes of Health and a fellowship from the Purdue Cancer Center. The associate editor coordinating the review of this manuscript and approving it for publication was Prof. Kannan Ramchandran.

S. Liu is with the Corporate Image Analysis Section, The Procter & Gamble Company, Cincinnati, OH 45252 USA.

E. J. Delp is with the Video and Image Processing Laboratory (VIPER), School of Electrical and Computer Engineering, Purdue University, West Lafayette, IN 47907-1285 USA (e-mail: ace@ecn.purdue.edu).

C. Babbs is with the Department of Basic Medical Sciences, School of Veterinary Medicine, Purdue University, West Lafayette, IN 47907-1285 USA.

Publisher Item Identifier S 1057-7149(01)01665-7.

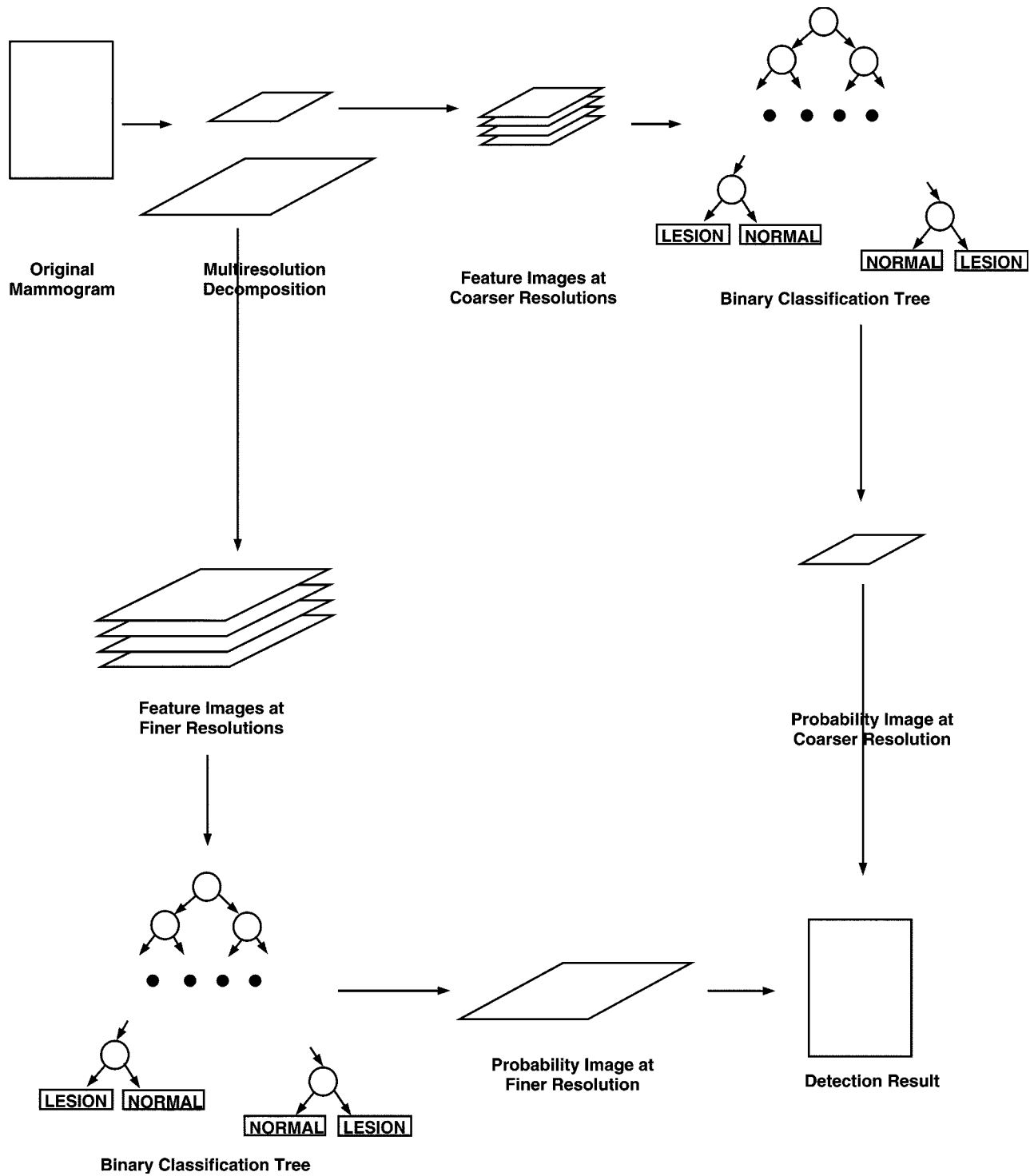


Fig. 1. Diagram of system for multiresolution spiculated lesion detection, illustrated here for only two resolutions—fine (left) and coarse (right).

II. MULTIREOLUTION DECOMPOSITION

As indicated above, the spiculated lesions we are interested in can occur in very different sizes. Hence, it is impossible to define *a priori* an optimal resolution for analyzing a mammogram. A multiresolution representation reorganizes image information into a set of details appearing at different spatial resolutions, and thus provides a hierarchical framework for image analysis [12]. Recently the wavelet transform has become a popular technique

for multiresolution representation and analysis in a wide variety of image processing applications, including computer aided diagnosis of mammograms [13]–[17].

We choose the linear phase nonseparable 2-D perfect reconstruction wavelet transform described in [18] to obtain a multiresolution representation [12] of the original mammogram. This transform does not introduce phase distortions in the decomposed images. In addition, no bias is introduced in the horizontal and vertical directions as would occur with a separable

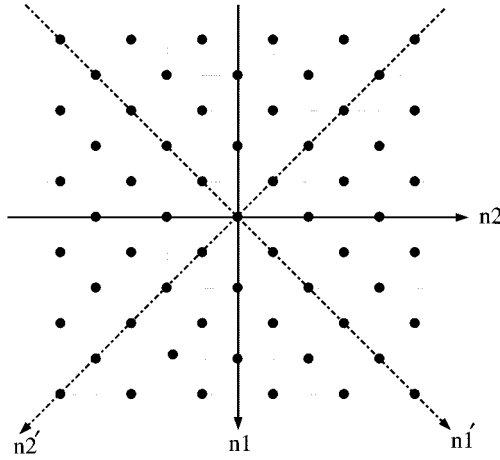


Fig. 2. Two-dimensional quincunx sublattice, used to create successive generations of lower resolution images for analysis.

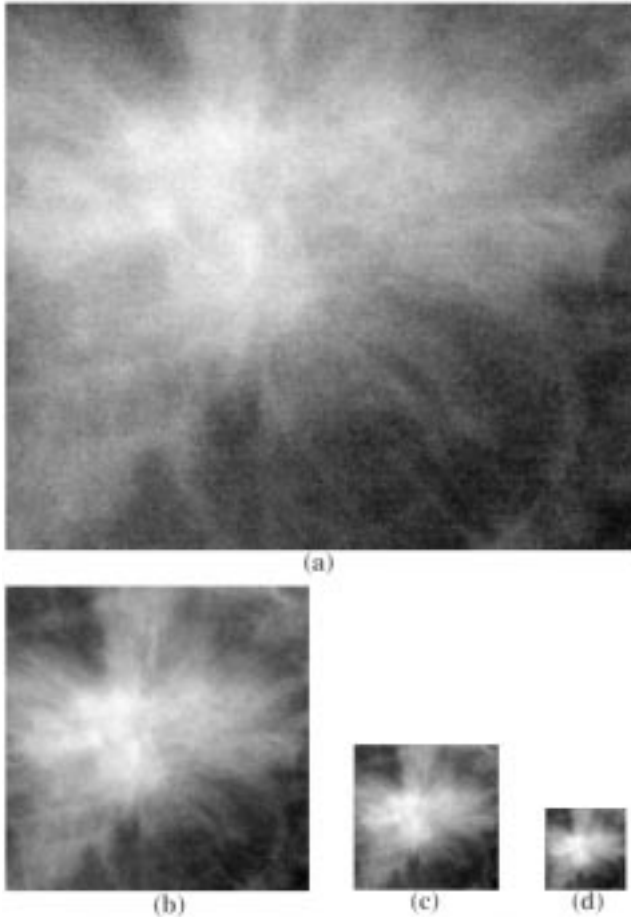


Fig. 3. Multiresolution representation of a spiculated lesion. (a) Speculated lesion as in the original mammogram of resolution $N \times N$. (b) In the coarser resolution $N/2 \times N/2$. (c) In the coarser resolution $N/4 \times N/4$. (d) In the coarsest resolution $N/8 \times N/8$.

transform. The impulse response of the analysis low pass filter is

$$h(n_1, n_2) = \begin{pmatrix} 0 & 0.125 & 0 \\ 0.125 & 0.5 & 0.125 \\ 0 & 0.125 & 0 \end{pmatrix}.$$

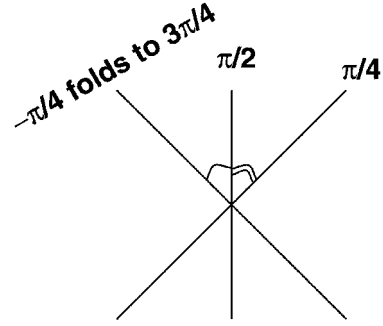


Fig. 4. Folding edge orientation makes the feature σ_{θ} insensitive to the nominal value of θ , but sensitive to the actual edge orientation variances.

The dilation matrix used to represent the subsampling lattice is

$$D = \begin{bmatrix} 1 & 1 \\ 1 & -1 \end{bmatrix}$$

which corresponds to the 2-D quincunx sublattice [18], as shown in Fig. 2.

Let the original mammogram have the finest resolution $N \times N$ pixels. Since D expands the sampling lattice by $\sqrt{2}$ in each direction, image resolution decreases by a factor of $1/\sqrt{2}$ after each decomposition. For example, the image at the second finest resolution has $N/\sqrt{2} \times N/\sqrt{2}$ pixels. We will use only images of spatial resolutions $(N \times N)$, $(N/2 \times N/2)$, \dots for feature extraction and classification.

III. MULTIREOLUTION FEATURE ANALYSIS

Spiculated lesions range in size from a few millimeters to several centimeters. Usually the larger the tumor center, the longer are the spicules or “arms” [19]. Hence a large lesion preserves a stellate appearance at several more coarse resolutions. This can be seen in Fig. 3, in which a spiculated lesion of 1 cm in radius is shown at multiple resolutions.

Also note that an $M \times M$ region at a coarser spatial resolution $N/n \times N/n$ corresponds to an $nM \times nM$ region in the original mammogram with spatial resolution $N \times N$. For example, if a set of features extracted within an 8×8 window in the original mammogram with spatial resolution $N \times N$ differentiates spiculated lesions of size ≈ 1 mm from normal tissue, then the same set of features extracted at the coarser resolution $N/4 \times N/4$, using the same sized 8×8 window, would be able to detect similar spiculated lesions of size ≈ 4 mm. This enables us to choose a fairly small neighborhood for feature extraction at the finest resolution and detect the smallest possible spiculated lesions. Larger lesions will be detected using the same set of features extracted at a coarser resolution. This strategy circumvents the difficulty of choosing a neighborhood size *a priori* to capture features of objects of varying sizes.

We extract four features from the low frequency wavelet coefficients for every pixel at each resolution. Let (i, j) be the spatial location in the mammogram at row i and column j ; $f(i, j)$ be the pixel brightness at (i, j) ; ∂S_{ij} be some neighborhood of (i, j) , and K be the number of pixels within ∂S_{ij} . The first two features are then defined as the following:

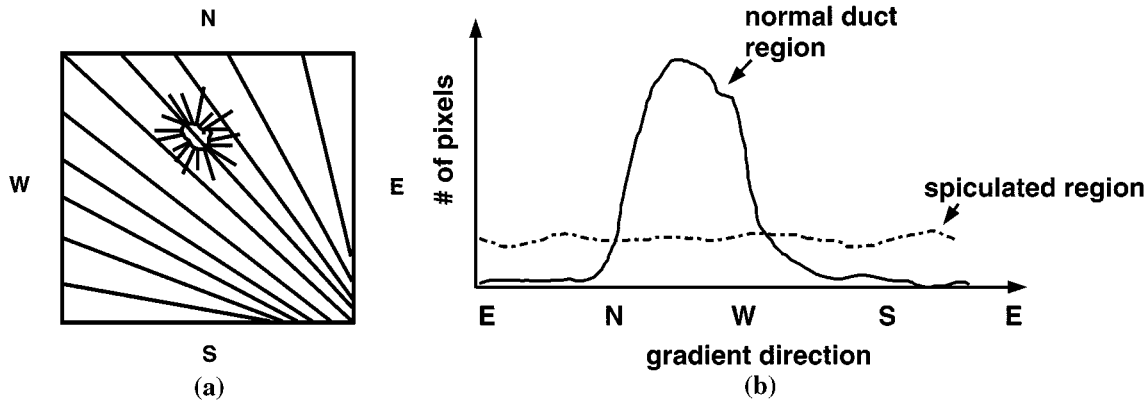


Fig. 5. (a) Directions of spicules of a spiculated lesion differ from the directions of normal linear markings in a mammogram and (b) standard deviation of gradient orientation histogram differentiates the area near a spiculated lesion from normal.

- mean pixel brightness in ∂S_{ij} :

$$\bar{f}(i, j) = \frac{1}{K} \sum_{(m, n) \in \partial S_{ij}} f(m, n);$$

- standard deviation of pixel brightnesses in ∂S_{ij} :

$$\sigma_f(i, j) = \sqrt{\frac{1}{K-1} \sum_{(m, n) \in \partial S_{ij}} (f(m, n) - \bar{f}(i, j))^2}.$$

Let $D_y(i, j)$ and $D_x(i, j)$ be an estimate of the vertical and horizontal spatial derivatives of f at (i, j) , respectively. Let $\theta(i, j) = \tan^{-1}\{D_y(i, j)/D_x(i, j)\}$ be an estimate of the gradient orientation at (i, j) with value $\in (-\pi/2, \pi/2]$. Also let $hist_{ij}$ be the histogram of θ within ∂S_{ij} using 256 bins, hence $hist_{ij}(n) = \#$ of pixels in ∂S_{ij} that have gradient orientations $\in (-\pi/2 + n\pi/256, -\pi/2 + (n+1)\pi/256]$, where $n = 0, 1, \dots, 255$. Let $\bar{hist}(i, j) = (1/256) \sum_{n=0}^{255} hist_{ij}(n)$ be the average bin height of $hist_{ij}$.

The third feature is defined as

- standard deviation of gradient orientation histogram in ∂S_{ij} :

$$\sigma_{hist}(i, j) = \sqrt{\frac{1}{255} \sum_{n=0}^{255} (hist_{ij}(n) - \bar{hist}(i, j))^2}.$$

Note that this feature is the same as the ALOE feature described in [8].

Let $K_{\theta_+}(i, j)$ and $K_{\theta_-}(i, j)$ be the number of positive and negative gradient orientations within ∂S_{ij} , respectively; $\bar{\theta}_+(i, j) = (1/K_{\theta_+}(i, j)) \sum_{\theta(m, n) \geq 0, (m, n) \in \partial S_{ij}} \theta(m, n)$ and $\bar{\theta}_-(i, j) = (1/K_{\theta_-}(i, j)) \sum_{\theta(m, n) < 0, (m, n) \in \partial S_{ij}} \theta(m, n)$ be the average positive and negative gradient orientations within ∂S_{ij} , respectively.

The folded gradient orientation $\theta'(i, j)$ at (i, j) is defined as:

$$\theta'(i, j) = \begin{cases} \theta(i, j) + \pi, & \text{if } \bar{\theta}_+(i, j) - \theta(i, j) > \frac{\pi}{2} \\ & \text{and } K_{\theta_+}(i, j) \geq K_{\theta_-}(i, j) \\ \theta(i, j) - \pi, & \text{if } \theta(i, j) - \bar{\theta}_-(i, j) > \frac{\pi}{2} \\ & \text{and } K_{\theta_+}(i, j) < K_{\theta_-}(i, j) \\ \theta(i, j), & \text{otherwise.} \end{cases}$$

And the fourth feature is then defined as:

- standard deviation of the folded gradient orientations in ∂S_{ij} :

$$\sigma_{\theta'}(i, j) = \sqrt{\frac{1}{K-1} \sum_{(m, n) \in \partial S_{ij}} (\theta'(m, n) - \bar{\theta'}(i, j))^2}.$$

This modification of θ to θ' in generating $\sigma_{\theta'}$ is necessary for this feature not to be sensitive to the nominal value of θ , but to the actual gradient orientation variances. As one can see from Fig. 4, the gradient orientation distance between $\pi/2$ and $-\pi/4$ is the same as that between $\pi/2$ and $\pi/4$. For our purpose of detecting spicules, we would like to obtain similar feature values for these two cases. However, if the θ s are used directly, a much larger variance for the former pair would result (2.8 versus 0.3); while using the folded gradient orientations θ' s, $-\pi/4$ will be folded to $3\pi/4$ and so we obtain the same $\sigma_{\theta'}$ for both cases. This feature is different than a similar one we presented in [14] and has proved to better characterize spiculated lesions. More information describing the feature set can be found in [20].¹

The features σ_{hist} and $\sigma_{\theta'}$ are chosen to be especially responsive to spiculated lesions. As illustrated in Fig. 5, a spiculated lesion differs from the normal ducts and connective tissue septae of the breast that tend to radiate from the nipple to the chest wall. It appears as an irregular tumor center surrounded by spicules that radiate in all directions. Accordingly, pixels in normal areas have rather similar gradient orientations, while pixels near spiculated lesions tend to have gradient orientations in many directions. Therefore, the standard deviation of gradient orientations in the neighborhood of a lesion pixel will be larger than that

¹This reference is available at <http://www.ece.purdue.edu/~ace>

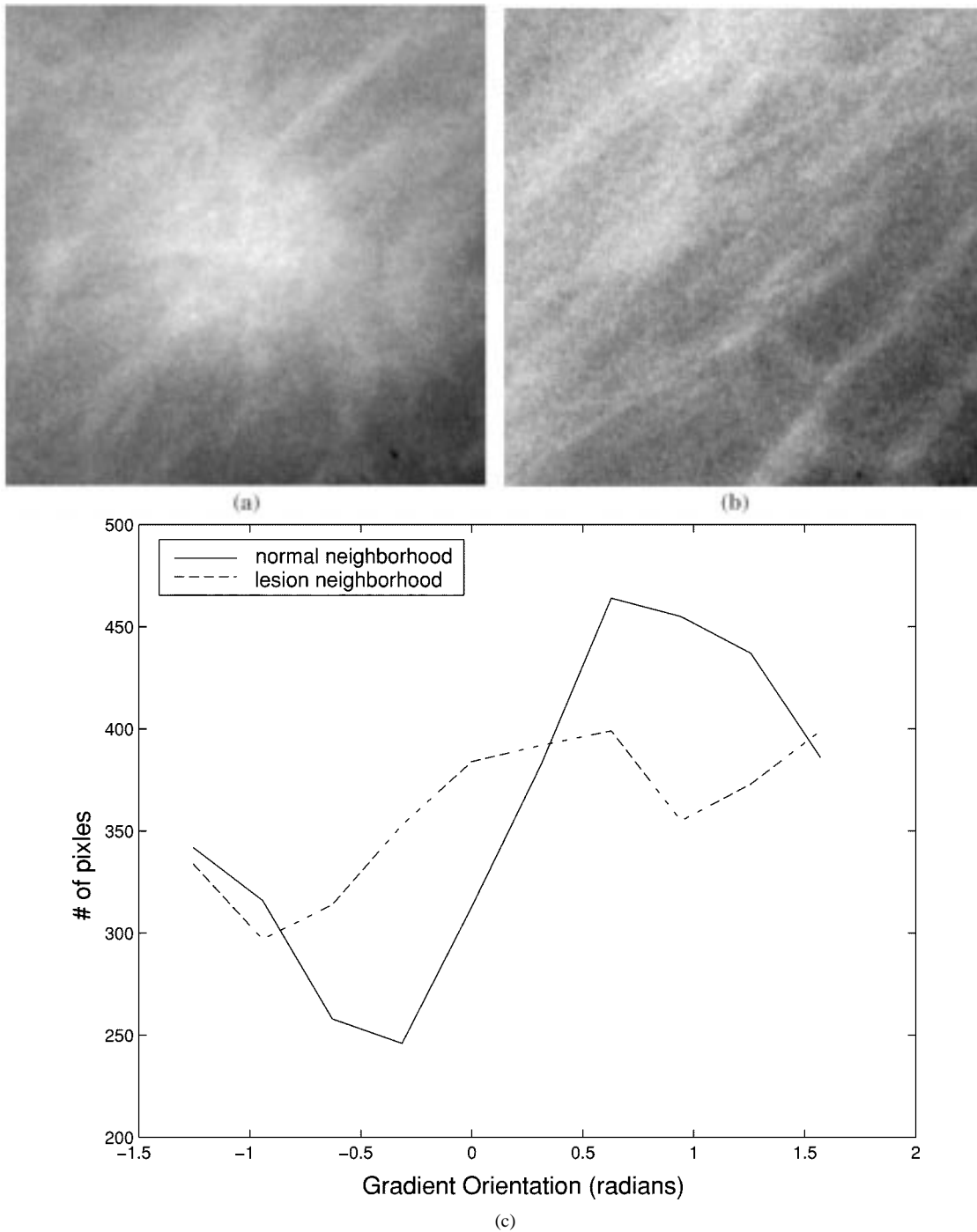


Fig. 6. (a) Spiculated lesion region, (b) normal region, and (c) gradient orientation histograms of (a) and (b).

in the neighborhood of a normal pixel. For the same reason, the gradient orientation histogram will be flat near a lesion pixel, but will have a peak corresponding to normal structure orientations near a normal pixel [8]. This result is shown in Fig. 6 which compares the gradient orientation histograms within a spiculated lesion region and within a normal region, respectively. The mean \bar{f} and standard deviation σ_f of the pixel brightnesses help further to differentiate lesions from normal tissue regions, because lesions usually have higher density, or appear brighter, in mammograms.

Fig. 7 shows a test pattern at multiple resolutions, which consists of an idealized spiculated lesion and parallel linear mark-

ings, embedded in uncorrelated Gaussian distributed noise with peak signal to noise ratio (PSNR) of 7 db. The lesion has a radius of 128 pixels in the original image. Figs. 8–11 show the features $\sigma_{\theta'}$, σ_{hist} , \bar{f} , and σ_f , respectively, for this test pattern. Each feature at different resolutions is extracted within same sized circular neighborhoods. For this test pattern, the neighborhood radius is 30 pixels for features $\sigma_{\theta'}$ and σ_{hist} , and 20 pixels for features \bar{f} and σ_f . A larger neighborhood size is used for features $\sigma_{\theta'}$ and σ_{hist} because they respond stronger to a spiculated lesion if the entire halo of spicules is included in the feature extraction window, while features \bar{f} and σ_f respond better to the central mass of the lesion. These features are able to dif-

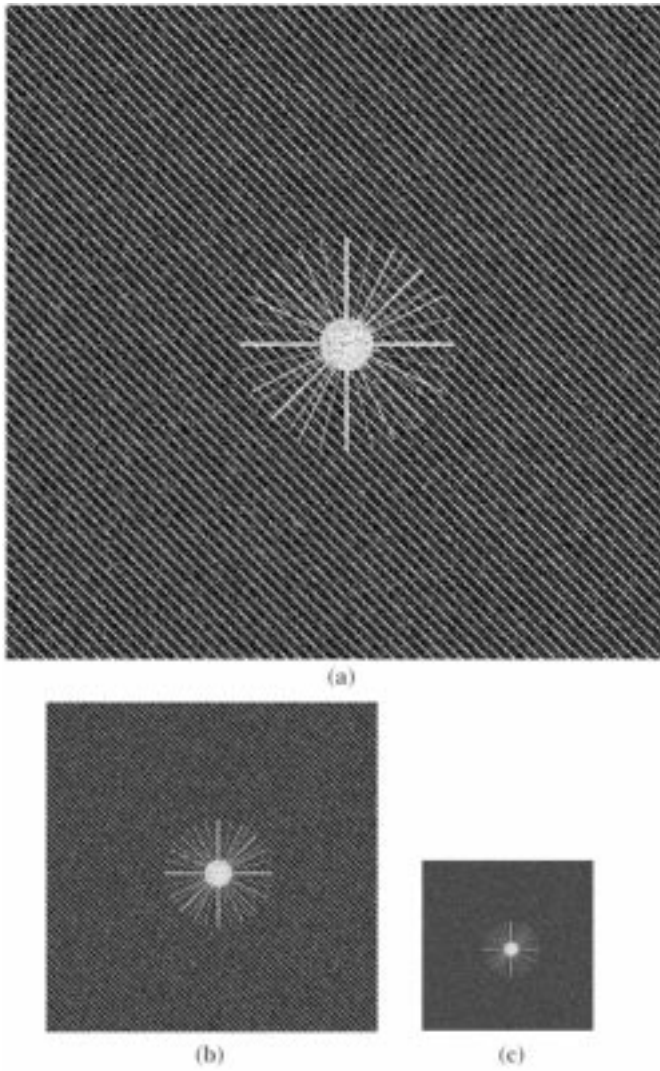


Fig. 7. Multiresolution representation of a test pattern consisting of an idealized spiculated lesion and normal structures embedded in uncorrelated Gaussian distributed noise. The lesion has a radius of 128 pixels in the original image. (a) Original $N \times N$ image, (b) coarser resolution $N/2 \times N/2$, and (c) coarsest resolution $N/4 \times N/4$.

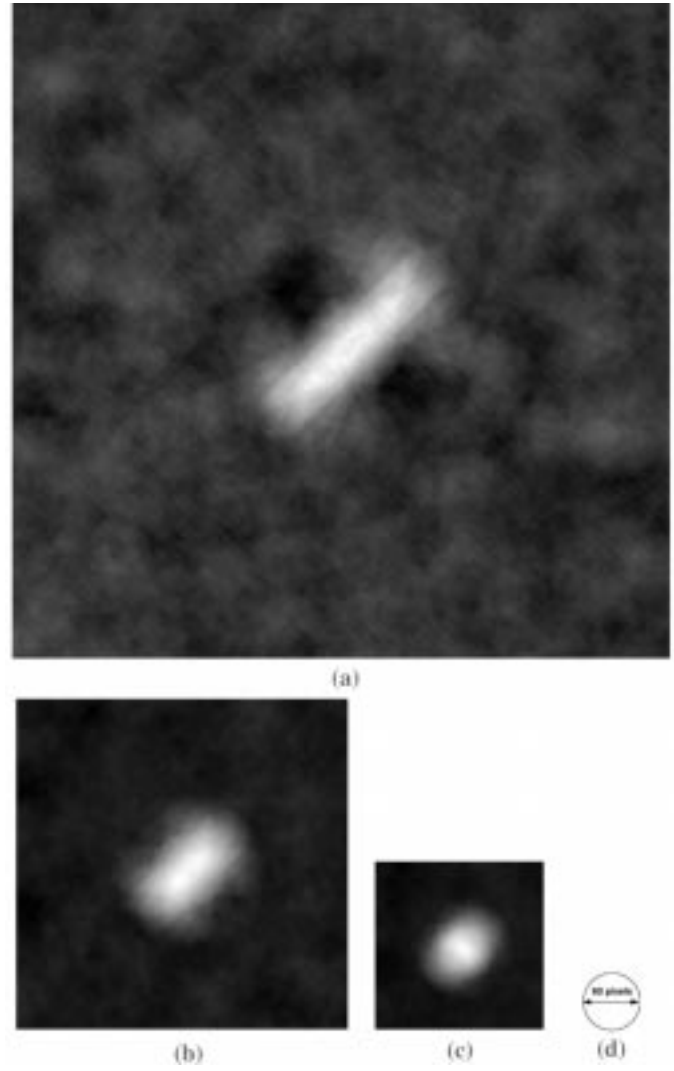


Fig. 8. Feature σ_{ϕ}^l obtained in circular neighborhoods of radius 30 pixels at all resolutions for the test pattern shown in Fig. 7. Here, large values (bright pixels) indicate spiculated regions as explained in Fig. 5. (a) Original $N \times N$ image. (b) Coarser resolution $N/2 \times N/2$. (c) Coarsest resolution $N/4 \times N/4$. (d) Circular neighborhood of size 30 pixels in radius.

ferentiate a spiculated lesion from a complex background. From Figs. 8 and 9, we can see that the features best discriminate the lesion from its background at resolution $(N/4 \times N/4)$ when the size of the feature extraction neighborhood matches that of the lesion. In this case, the brightest spot in the feature image in Fig. 8(c) and the darkest spot in the feature image in Fig. 9(c) directly overlay both the central mass and the spicules of the lesion.

IV. CLASSIFICATION ALGORITHM

A sequential hierarchical decision scheme has been shown to achieve better performance than employing a single “best” set of features in a one-step decision [21], [22]. A binary classification tree (BCT) is simple, fast, and efficient type of hierarchical classifier. Fig. 12 shows a simple BCT with three features and two classes where circular nodes are binary decision nodes and square nodes are terminal nodes with class labels assigned. When an unknown feature vector is submitted for classification,

it will first go to the root node, which is always a binary decision node, and then take one of the two branches based on the outcome of testing one of its features against the threshold at that binary decision node. This process continues until the feature vector reaches one of the terminal nodes where it is assigned a class label. This tree structured classification approach has several advantages over more traditional nonparametric methods such as the nearest neighbor method [21].

- 1) BCT does automatic stepwise feature selection and complexity reduction;
- 2) BCT is robust with respect to outliers and misclassified points in the training set;
- 3) final classifier can be compactly stored;
- 4) BCT efficiently classifies new data;
- 5) BCT provides easily understood and interpreted information regarding the predictive structure of the data.

We choose the iterative growing and pruning algorithm proposed in [22] for our classification tree design because it not

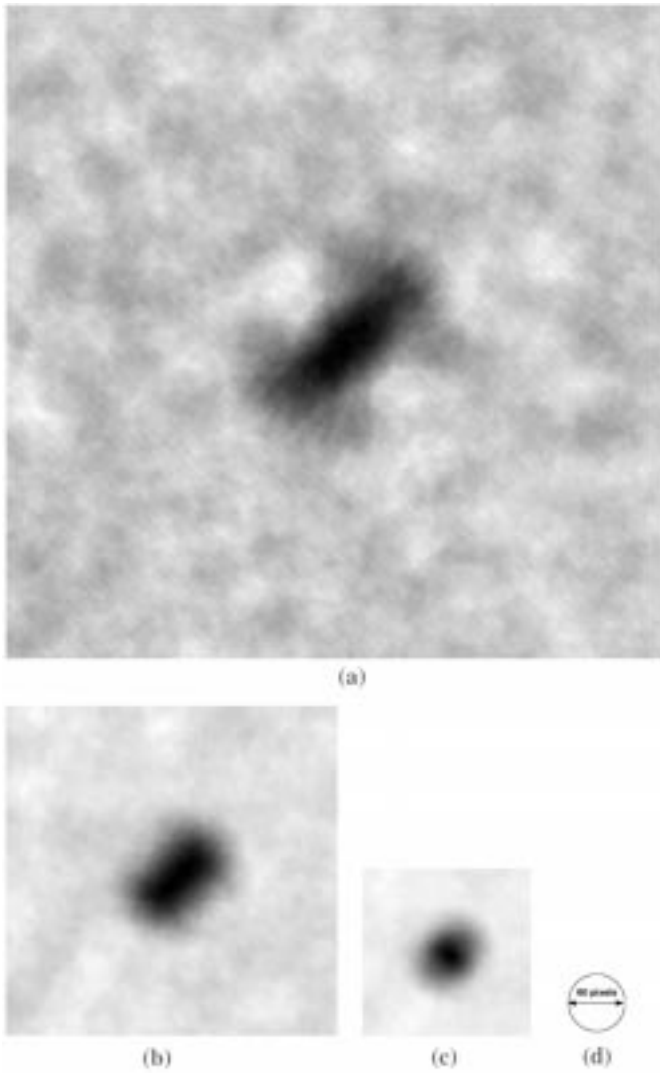


Fig. 9. Feature σ_{hist} obtained in circular neighborhoods of radius 30 pixels at all resolutions for the test pattern shown in Fig. 7. Here, small values (dark pixels) indicate spiculated regions as explained in Fig. 5. (a) Original $N \times N$ image. (b) Coarser resolution $N/2 \times N/2$. (c) Coarsest resolution $N/4 \times N/4$. (d) Circular neighborhood of size 30 pixels in radius.

only produces trees with higher classification accuracy, but also requires less computation than other widely used tree design algorithms, such as CART [21].

Considering that there is redundancy in mapping the feature space by spatially adjacent samples, only a subsampling of the training set is used to grow BCT. After the BCT is generated, we associate with each terminal node a suspicious probability which is the percentage of lesion pixels in the training images that falls in this terminal node. The suspicious probability is then recomputed using the entire set of training samples. This partly compensates for the lost classification accuracy due to the fact that not all the training samples are used to design the tree [8].

At each resolution, five features are used for classification: the four features extracted at that resolution plus the feature $\sigma_{hist,i,j}$ extracted at the next coarser resolution. Our experiments have shown that using features across resolutions simultaneously helps capture spiculated lesions of varying sizes. Detection starts from the second coarsest resolution and then goes

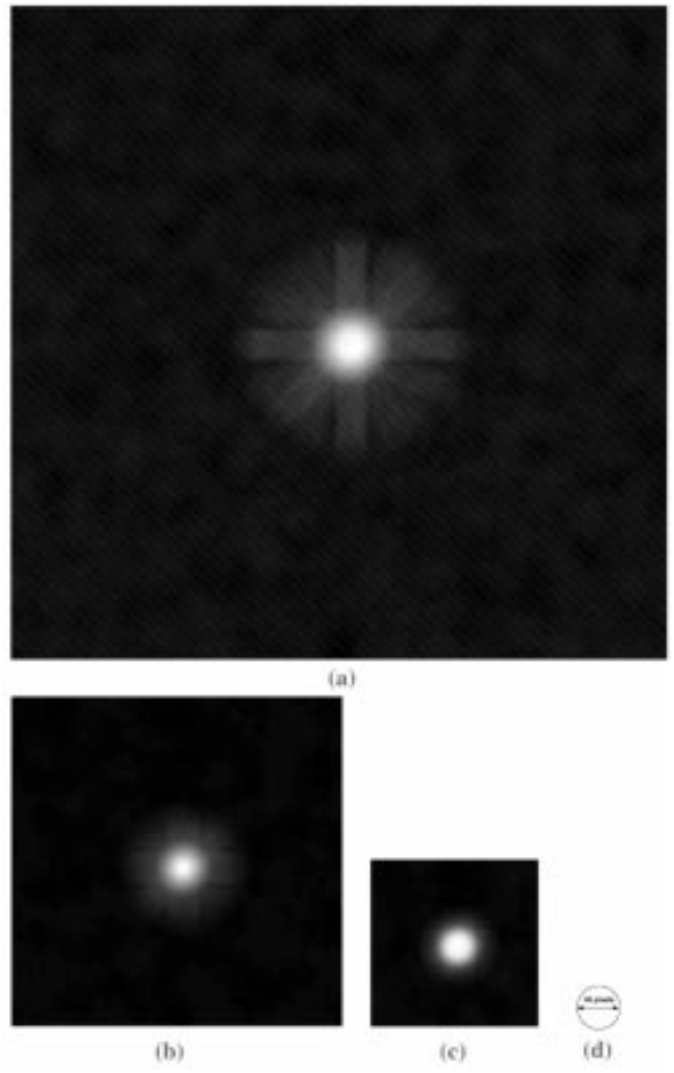


Fig. 10. Feature \bar{f} obtained in circular neighborhoods of radius 20 pixels at all resolutions for the test pattern shown in Fig. 7: (a) Original $N \times N$ image. (b) Coarser resolution $N/2 \times N/2$. (c) Coarsest resolution $N/4 \times N/4$. (d) Circular neighborhood of size 20 pixels in radius.

to the next finer resolution until the original mammogram is reached. A positive detection at a coarser resolution propagates to finer resolutions, which effectively reduces the number of pixels to be classified. A negative result at a coarser resolution will be combined with those at finer resolutions via a weighted sum.

We obtain a probability image from the BCT for each test mammogram, in which the pixel values represent the probability that a pixel belongs to a spiculated lesion. A median filter is then used to eliminate isolated positive responses, followed by a smoothing filter to reach a consensus within neighboring pixels. Final results are obtained by thresholding the filtered probability image.

V. EXPERIMENTAL RESULTS AND DISCUSSIONS

We tested the proposed multiresolution detection algorithm on the MIAS database [23] provided by the Mammographic Image Analysis Society (MIAS) in the U.K. Images in the MIAS

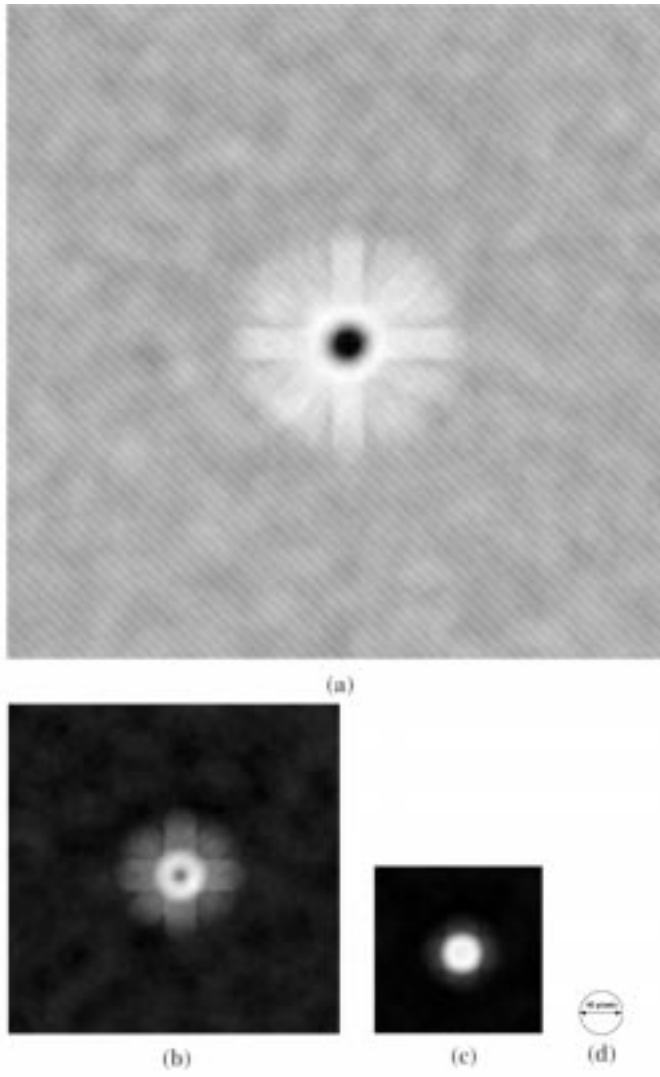


Fig. 11. Feature σ_f obtained in circular neighborhoods of radius 20 pixels at all resolutions for the test pattern shown in Fig. 7. Note that feature values get smaller (darker) in the background area at coarser resolutions because of the smoothing effect of the lowpass filtering step in obtaining coarser resolution images. (a) Original $N \times N$ image. (b) Coarser resolution $N/2 \times N/2$. (c) Coarsest resolution $N/4 \times N/4$. (d) Circular neighborhood of size 20 pixels in radius.

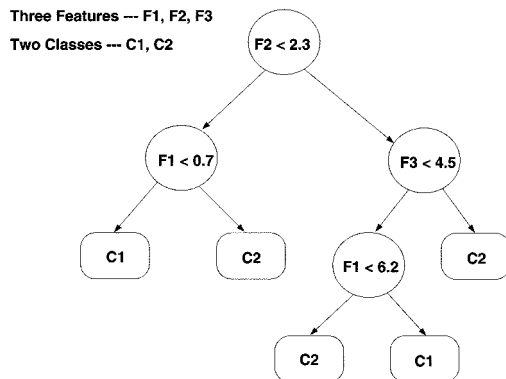


Fig. 12. A simple binary classification tree with three features and two classes. The circular nodes are binary decision nodes and the square nodes are terminal nodes with class labels assigned.

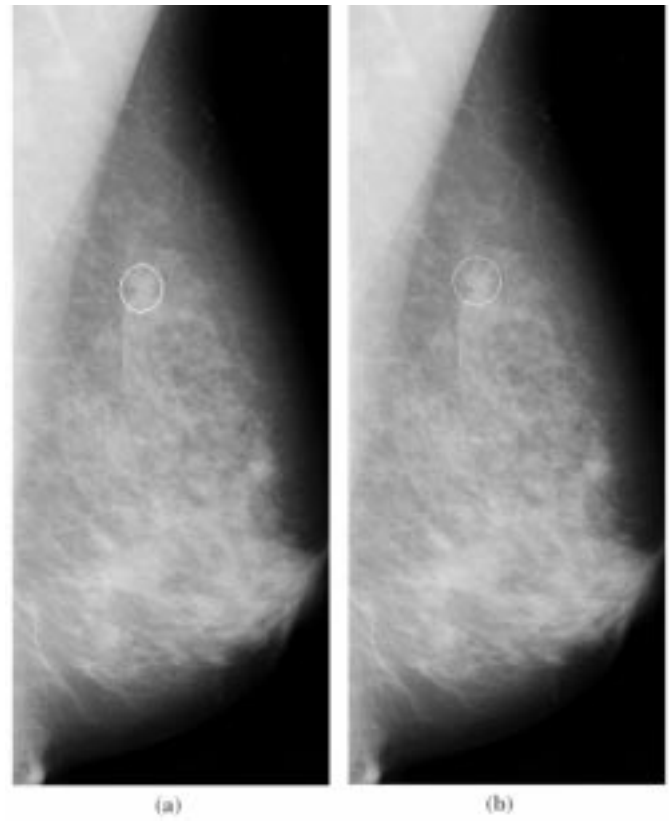


Fig. 13. Spiculated lesion of size 6.6 mm detected at the finest resolution (a) Mammogram with automatic detection and (b) mammogram with tumor as determined by expert radiologists.

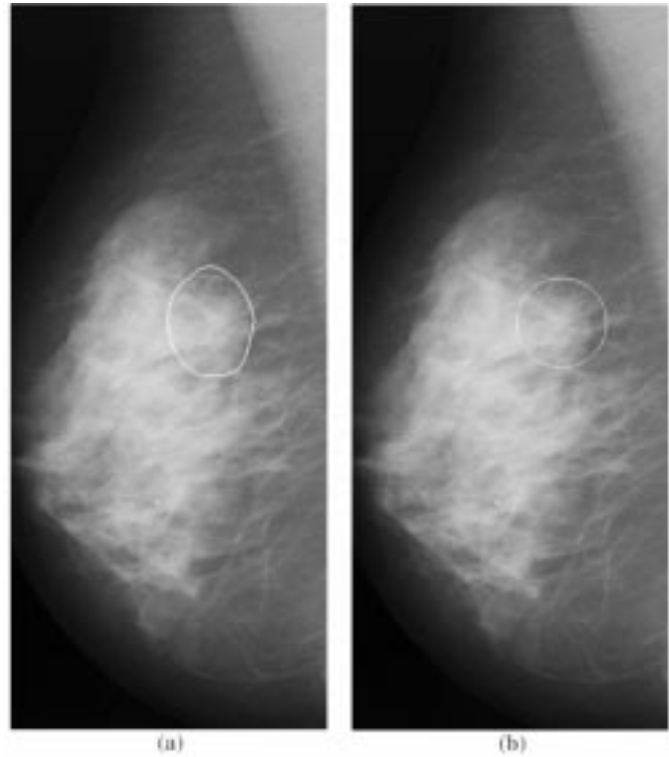


Fig. 14. Spiculated lesion of size 12.4 mm detected at the second coarsest resolution. (a) Mammogram with automatic detection and (b) mammogram with tumor as determined by expert radiologists.

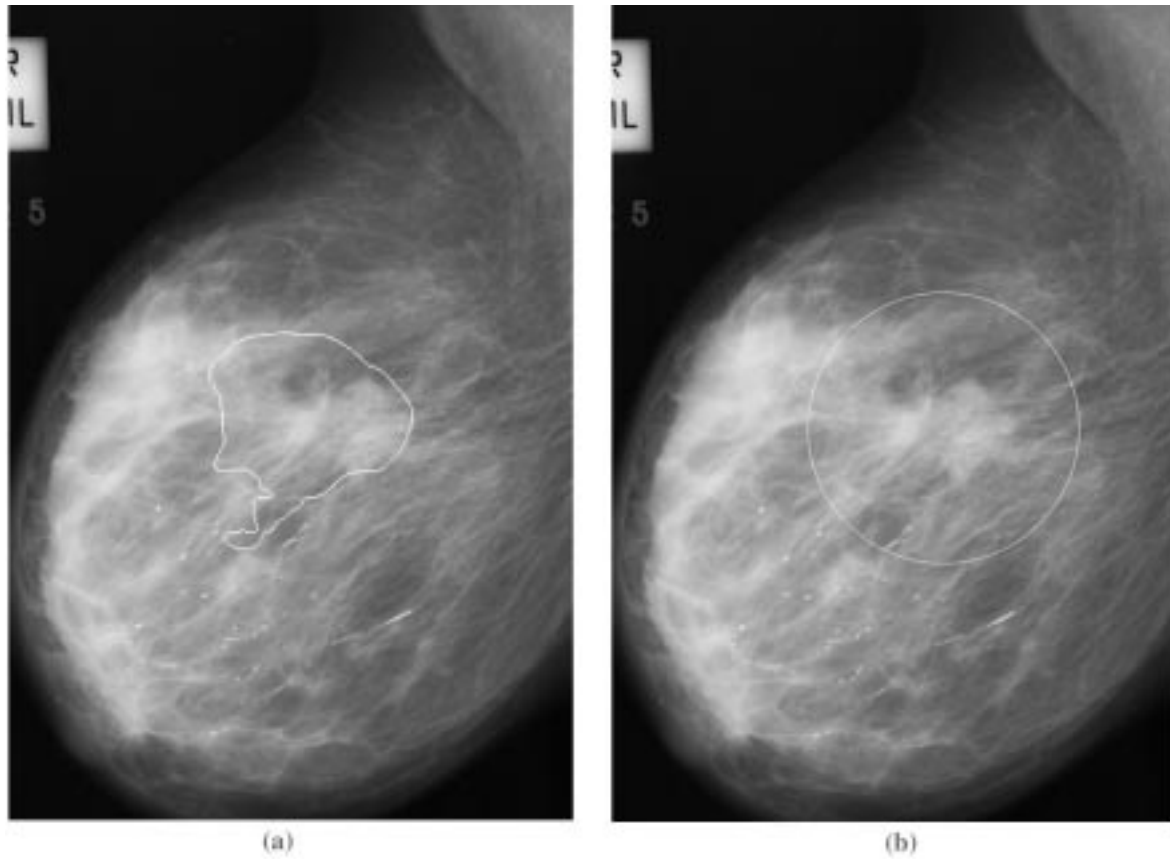


Fig. 15. Spiculated lesion of size 35 mm detected at the coarsest resolution. (a) Mammogram with automatic detection and (b) mammogram with tumor as determined by expert radiologists.

database have 50-micron resolution. There is a total of 19 mammograms containing spiculated lesions. The smallest lesion extends 3.6 mm in radius, while the biggest one is nearly ten times larger and extends to 35 mm. These 19 together with another 19 normal mammograms, also taken from the MIAS database, were randomly split into two sets with approximately an equal number of lesions and normal mammograms in each set. Each set was then used separately as a training set to generate two BCTs, according to a split-half training paradigm similar to Kegelmeyer *et al.* [8]. A BCT trained by one set was used to classify mammograms in the other set, and vice versa. Therefore, no mammogram was used both for training and testing.

The wavelet transform described in Section II was used to generate the multiresolution representations of each mammogram. Features described in Section III were extracted from images of spatial resolutions $(N \times N)$, $(N/2 \times N/2)$, $(N/4 \times N/4)$, and $(N/8 \times N/8)$. Circular regions were used for all feature extractions so that features behave equally in all directions. In this experiment, the neighborhood radius for extracting features σ_θ and σ_{hist} was 60 at all resolutions, which corresponds to a radius of 3 mm, 6 mm, 12 mm, and 24 mm in the original resolution $(N \times N)$, and coarser resolutions $(N/2 \times N/2)$, $(N/4 \times N/4)$, and $(N/8 \times N/8)$, respectively. The neighborhood radius for extracting features \hat{f} and σ_f was 20 at all resolutions, which corresponds to a radius of 1 mm, 2 mm, 4 mm, and 8 mm in the original resolution $(N \times N)$, and coarser resolutions $(N/2 \times N/2)$, $(N/4 \times N/4)$, and $(N/8 \times N/8)$, respectively. Extracting fea-

tures at coarser resolutions for relatively large regions significantly reduces the amount of computation.

Accordingly, three-level classifications were performed for each mammogram, starting from resolution $(N/4 \times N/4)$ and going to $(N \times N)$. At each resolution, the corresponding five dimensional feature vector, including the four features extracted at that resolution and σ_{hist} extracted at the next coarser resolution, was classified through the BCT trained by the other half test set. The output is a probability image, in which the pixel values represent the probability of belonging to spiculated lesions. We then used a median filter of radius 5 to eliminate isolated positive responses, followed by a smoothing filter to reach a consensus within neighboring pixels. Because we are looking for larger lesions at coarser resolutions and smaller ones at finer resolutions, the radii used for smoothing filters were chosen to be 18 mm, 6 mm, and 2 mm at resolutions $(N/4 \times N/4)$, $(N/2 \times N/2)$, and $(N \times N)$, respectively. The detection result was obtained by thresholding the smoothed probability image. Using a small threshold is more likely to detect true lesions, but also to generate more false positive responses. Using a large threshold gives fewer false positive responses, but may miss more true lesions. Hence variation of thresholds gives different diagnostic accuracy which can be quantified using free response receiver operating characteristic (FROC) analysis [24], where the true positive fraction (TPF) is plotted as a function of the average number of false positives (FP) per image. FROC analysis [24] is well suited for the assessment of computer aided

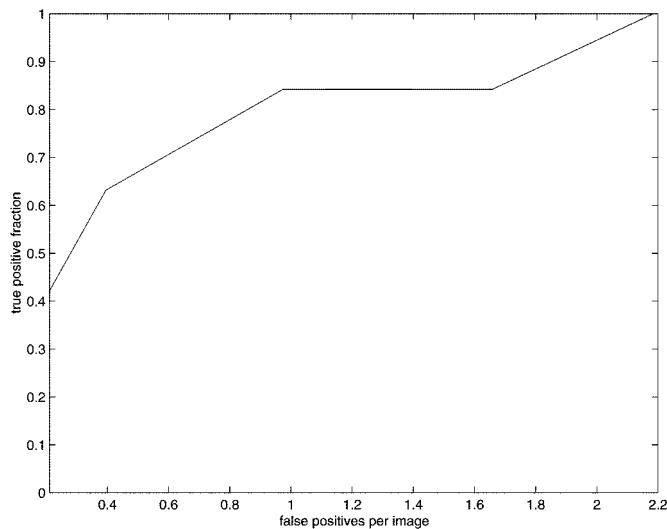


Fig. 16. FROC curve for detection of spiculated lesions in the MIAS database.

diagnosis of mammograms because it is applicable to situations that involve any number of reported locations and any number of actual lesions in each image.

If there is a positive detection at a coarser resolution, no feature extraction and detection are needed at the corresponding pixel locations at all finer resolutions. This approach effectively reduces the number of pixels to be classified. Smaller probabilities that give negative responses are propagated to finer resolutions by weighted sum. Fig. 13 shows a spiculated lesion of size 6.6 mm detected at the finest original resolution; Fig. 14 shows a spiculated lesion of size 12.4 mm detected at the second coarsest resolution; and Fig. 15 shows a spiculated lesion of size 35 mm detected at the coarsest resolution.

The coarse to fine detection scheme speeds up computation in two ways. First, positive responses at lower resolutions effectively reduces computation at higher resolutions. Secondly, most of the computation is saved by allowing feature extraction within small windows. For example, we only need a 40×40 pixel window for feature extraction in 2 mm, 4 mm, and 8 mm neighborhoods in a $50\text{-}\mu$ mammogram, because we extract features at different resolutions. If we extracted features in the original image in three spatial scales so as to examine different sizes of possible spiculated lesions, similar to Karssemeijer and Brake [11], the 2 mm, 4 mm, and 8 mm neighborhoods would correspond to 40×40 , 80×80 , and 160×160 pixel window sizes, respectively, which would cost at least 600% more computation.

To evaluate the computer diagnosis results, we adopted the criteria in [8]: a computer finding is considered as a true positive detection if its area is overlapped by at least 50% of a true lesion as indicated by an expert radiologist; a computer finding that does not so overlap a true lesion is considered as false positive; and a true lesion that is not overlapped by any computer finding is considered as false negative. By these criteria, the diagnostic accuracy performance of our algorithm on the MIAS database quantified using FROC curve is shown in Fig. 16. We achieved 84.2% true positive detection at less than 1 false positive per image and 100% true positive detection at 2.2 false positive per image. The spiculated lesion that was missed first when the de-

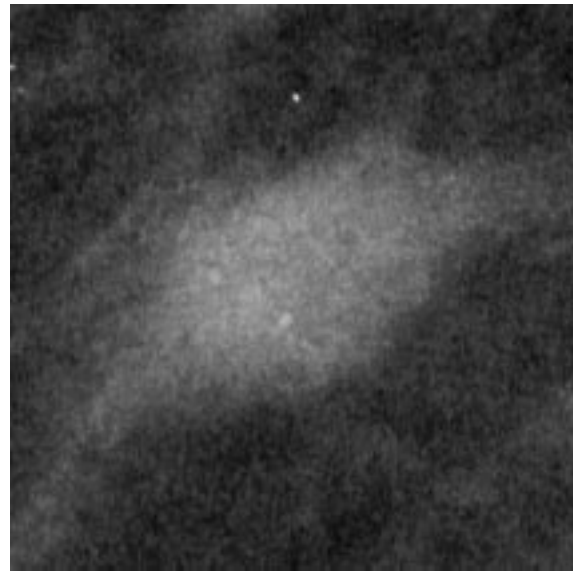


Fig. 17. The first missed spiculated lesion when the detection sensitivity is decreased. It lacks visible spicules at all directions.

tection threshold was increased, or the sensitivity decreased, is shown in Fig. 17. This lesion lacks visible spicules at all directions. Karssemeijer and Brake [11] reported comparable results on the MIAS database—around 90% true positive detection at one false positive per image and 100% true positive detection at more than four false positive per image. The presented multiresolution algorithm for the detection of spiculated lesions in digital mammograms is capable of detecting spiculated lesions of very different sizes at low false positive rates.

ACKNOWLEDGMENT

The authors would like to thank Dr. V. P. Jackson, the J. A. Campbell Prof. of Radiology at Indiana University, and Prof. Z. Pizlo of the Department of Psychological Sciences at Purdue University, for their helpful suggestions.

REFERENCES

- [1] D. B. Kopans, *Breast Imaging*. New York: Lippincott, 1989.
- [2] L. W. Bassett, V. P. Jackson, R. Jahan, Y. S. Fu, and R. H. Gold, *Diagnosis of Diseases of the Breast*. Philadelphia, PA: Saunders, 1997.
- [3] G. Cardenosa, "Mammography: An overview," in *Proc. 3rd Int. Workshop Digital Mammography*, Chicago, IL, June 9–12, 1996, pp. 3–10.
- [4] K. Woods and K. Bowyer, "A general view of detection algorithms," in *Proc. 3rd Int. Workshop Digital Mammography*, Chicago, IL, June 9–12, 1996, pp. 385–390.
- [5] M. L. Giger, F.-F. Yin, K. Doi, C. E. Metz, R. A. Schmidt, and C. J. Vyborny, "Investigation of methods for the computerized detection and analysis of mammographic masses," *Proc. SPIE*, pp. 183–184, Feb. 6–8, 1990.
- [6] N. Karssemeijer, "A stochastic model for automated detection of calcifications in digital mammograms," in *12th Int. Conf. Information Processing Medical Imaging*, Wye, U.K., 1991, pp. 227–238.
- [7] C. J. Vyborny and M. L. Giger, "Computer vision and artificial intelligence in mammography," *Amer. J. Roentgenology*, vol. 162, pp. 699–708, Mar. 1994.
- [8] W. P. Kegelmeyer Jr., J. M. Pruneda, P. D. Bourland, A. Hillis, M. W. Riggs, and M. L. Nipper, "Computer-aided mammographic screening for spiculated lesions," *Radiology*, vol. 191, pp. 331–336, May 1994.
- [9] M. L. Comer, S. Liu, and E. J. Delp, "Statistical segmentation of mammograms," in *Proc. 3rd Int. Workshop Digital Mammography*, Chicago, IL, June 9–12, 1996, pp. 475–478.

- [10] W. P. Kegelmeyer Jr., "Computer detection of stellate lesions in mammograms," in *Proc. SPIE Conf. Biomedical Image Processing Three-Dimensional Microscopy*, San Jose, CA, Feb. 10–13, 1992, pp. 446–454.
- [11] N. Karssemeijer and G. M. Brake, "Detection of stellate distortions in mammograms," *IEEE Trans. Med. Imag.*, vol. 15, pp. 611–619, Oct. 1996.
- [12] S. G. Mallat, "A theory for multiresolution signal decomposition: The wavelet representation," *IEEE Trans. Pattern Anal. Machine Intell.*, vol. 11, pp. 674–693, July 1989.
- [13] M. Unser and A. Aldroubi, "A review of wavelets in biomedical applications," *Proc. IEEE*, vol. 84, pp. 626–638, Apr. 1996.
- [14] S. Liu and E. J. Delp, "Multiresolution detection of stellate lesions in mammograms," in *Proc. IEEE Int. Conf. Image Processing*, Santa Barbara, CA, Oct. 26–29, 1997, pp. 109–112.
- [15] R. N. Strickland and H. I. Hahn, "Wavelet transforms for detecting microcalcifications in mammograms," *IEEE Trans. Med. Imag.*, vol. 15, pp. 218–229, Apr. 1996.
- [16] A. F. Laine, S. Schuler, J. Fan, and W. Huda, "Mammographic feature enhancement by multiscale analysis," *IEEE Trans. Med. Imag.*, vol. 13, pp. 725–752, Dec. 1994.
- [17] C. H. Chen and G. G. Lee, "Image segmentation using multiresolution wavelet analysis and expectation-maximization (EM) algorithm for digital mammography," *Int. J. Imag. Syst. Technol.*, vol. 8, no. 5, pp. 491–504, 1997.
- [18] J. Kováčević and M. Vetterli, "Nonseparable multidimensional perfect reconstruction filter banks and wavelet bases for R^n ," *IEEE Trans. Inform. Theory*, vol. 38, pp. 533–555, Mar. 1992.
- [19] L. Tabar and P. B. Dean, *Teaching Atlas of Mammography*, 2nd ed. Berlin, Germany: Georg Thieme Verlag, 1985.
- [20] S. Liu, "The analysis of digital mammograms: Speculated tumor detection and normal mammogram characterization," Ph.D. dissertation, Purdue Univ., West Lafayette, IN, May 1999.
- [21] L. Breiman, J. H. Friedman, R. A. Olshen, and C. J. Stone, *Classification and Regression Trees*. Belmont, CA: Wadsworth, 1984.
- [22] S. B. Gelfand, C. S. Ravishanker, and E. J. Delp, "An iterative growing and pruning algorithm for classification tree design," *IEEE Trans. Pattern Anal. Machine Intell.*, vol. 13, pp. 163–174, Feb. 1991.
- [23] J. Suckling, J. Parker, D. R. Dance, S. Astley, J. Hutt, C. R. M. Doggis, I. Ricketts, E. Stamatakis, N. Cerneaz, S. L. Kok, P. Taylor, D. Betal, and J. Savage, "The mammographic image analysis society digital mammogram database," in *Proc. 2nd Int. Workshop Digital Mammography*, York, U.K., July 10–12, 1994, pp. 375–378.
- [24] C. E. Metz, "Evaluation of digital mammography by ROC analysis," in *Proc. 3rd Int. Workshop Digital Mammography*, Chicago, IL, June 9–12, 1996, pp. 61–68.



Sheng Liu (S'95–M'99) received the B.S.E.E. (with highest honors) and M.S.E.E. degrees from Shanghai Jiao Tong University, China, in 1990 and 1992, respectively. She received the Ph.D. degree in electrical and computer engineering from Purdue University, West Lafayette, IN, in 1999.

From 1995 to 1999, she was supported by a National Institutes of Health Grant and a Purdue Cancer Center Research Foundation Fellowship for her research on tumor detection in mammograms. In 1993, she was a Researcher with the Department of Electronic Engineering, Shanghai Jiao Tong University, where her work included real time object recognition and video source coding. From 1994 to 1995, she was a Research Assistant with the Department of Electrical Engineering, University of Hawaii, Manoa, where her research was on parallel image compression and content-addressable image database systems. During the Summer of 1997 and Winter of 1998, she was a research intern at the Networked Image Technology Center (NITC), Eastman Kodak Company, Rochester, NY, where she conducted research on digital photo segmentation. She is currently a Research Scientist with the Corporate Image Analysis Section, The Procter & Gamble Company, Cincinnati, OH, where she is involved in the development of facial feature analysis systems. Her research interests include multiresolution signal analysis, medical imaging, image segmentation, and compression.

Dr. Liu is a member of Tau Beta Pi, Eta Kappa Nu, and Phi Kappa Phi.



Charles F. Babbs received the M.D. (with honors) and M.S. (anatomy) degrees from Baylor College of Medicine, Houston, TX, the Ph.D. degree in pharmacology from Purdue University, West Lafayette, IN, and the B.S. in experimental psychology from Yale University, New Haven, CT.

He is an Associate Research Scholar with the Department of Basic Medical Sciences and an Instructor in family medicine at Indiana University School of Medicine, Indianapolis. He has received an NIH Research Career Development Award, and has written

more than 150 refereed articles and ten chapters in scholarly journals and textbooks. His research is in the areas of biomedical engineering, cardiopulmonary resuscitation, tumor blood flow, heat therapy for cancer, digital mammography, the biochemistry of cellular damage after cardiac arrest, including the roles of free radicals and iron in reperfusion injury and the biomechanics of closed head injury.



Edward J. Delp (S'70–M'79–SM'86–F'97) was born in Cincinnati, OH. He received the B.S.E.E. (cum laude) and M.S. degrees from the University of Cincinnati, and the Ph.D. degree from Purdue University, West Lafayette, IN.

From 1980 to 1984, he was with the Department of Electrical and Computer Engineering, The University of Michigan, Ann Arbor. Since August 1984, he has been with the School of Electrical and Computer Engineering, Purdue University, where he is a Professor of Electrical and Computer Engineering. His research

interests include image and video compression, multimedia security, medical imaging, multimedia systems, communication, and information theory. He has also consulted for various companies and government agencies in the areas of signal and image processing, robot vision, pattern recognition, and secure communications. From 1984 to 1991, he was a member of the editorial board of the *International Journal of Cardiac Imaging*. Since 1992, has been a member of the editorial board of *Pattern Recognition*, and from 1994 to 2000, he was an Associate Editor of the *Journal of Electronic Imaging*. He is co-editor of the book *Digital Cardiac Imaging* (Amsterdam, The Netherlands: Martinus Nijhoff). During the Summers of 1998 and 1999, he was a Visiting Professor at the Tampere International Center for Signal Processing, Tampere University of Technology, Tampere, Finland. He is a registered Professional Engineer.

Dr. Delp is a member of Tau Beta Pi, Eta Kappa Nu, Phi Kappa Phi, Sigma Xi, ACM, and the Pattern Recognition Society. He is a Fellow of SPIE and the Society for Imaging Science and Technology (IS&T). In 2000, he was selected as a Distinguished Lecturer of the IEEE Signal Processing Society. From 1997 to 1999, he was Chair of the Image and Multidimensional Signal Processing (IMDSP) Technical Committee of the IEEE Signal Processing Society. He was Program Chair of the IEEE Signal Processing Society's Ninth IMDSP Workshop held in Belize in March 1996. He is the Program Co-Chair of the IEEE International Conference on Image Processing that will be held in Barcelona, Spain, in 2003. From 1991 to 1993, he was an Associate Editor of the IEEE TRANSACTIONS ON PATTERN ANALYSIS AND MACHINE INTELLIGENCE. From 1996 to 1998, he was an Associate Editor of the IEEE TRANSACTIONS ON IMAGE PROCESSING. In 1990, he received the Honeywell Award and in 1992 the D. D. Ewing Award for excellence in teaching. In 1990 he received a Fulbright Fellowship to visit the Universitat Politècnica de Catalunya, Barcelona. He was Co-Chair of the SPIE/IS&T Conference on Security and Watermarking of Multimedia Contents, held in San Jose, CA, in January 1999, January 2000, and January 2001. He was the General Co-Chair of the 1997 Visual Communications and Image Processing Conference (VCIP) held in San Jose. From 1994 to 1998, he was Vice-President for Publications of IS&T. He was General Co-Chairman of the 1993 SPIE/IS&T Symposium on Electronic Imaging.